



INSTITUT DE FRANCE
Académie des sciences

Comptes Rendus

Géoscience

Sciences de la Planète


James Badro, Paolo A. Sossi, Zhengbin Deng, Stephan Borensztajn,
Nicolas Wehr and Frederick J. Ryerson

**Experimental investigation of elemental and isotopic evaporation
processes by laser heating in an aerodynamic levitation furnace**

Volume 353, issue 1 (2021), p. 101-114

<<https://doi.org/10.5802/crgeos.56>>

© Académie des sciences, Paris and the authors, 2021.
Some rights reserved.

 This article is licensed under the
CREATIVE COMMONS ATTRIBUTION 4.0 INTERNATIONAL LICENSE.
<http://creativecommons.org/licenses/by/4.0/>



*Les Comptes Rendus. Géoscience — Sciences de la Planète sont membres du
Centre Mersenne pour l'édition scientifique ouverte*
www.centre-mersenne.org



Original article — Petrology, Geochemistry

Experimental investigation of elemental and isotopic evaporation processes by laser heating in an aerodynamic levitation furnace

James Badro^{*,a}, Paolo A. Sossi^{a,b}, Zhengbin Deng^a, Stephan Borensztajn^a,
Nicolas Wehr^a and Frederick J. Ryerson^{a,c}

^a Université de Paris, Institut de Physique du Globe de Paris, CNRS, 75005 Paris, France

^b Institut für Geochemie und Petrologie, ETH Zürich, 8092 Zürich, Switzerland

^c Lawrence Livermore National Laboratory, Livermore, CA 94550, USA

Current address: Centre for Star and Planet Formation, Globe Institute, University of Copenhagen, Copenhagen, Denmark (Z. Deng)

E-mails: badro@ipgp.fr (J. Badro), paolo.sossi@erdw.ethz.ch (P. A. Sossi), zhengbin.deng@sund.ku.dk (Z. Deng), borensztajn@ipgp.fr (S. Borensztajn), wehr@ipgp.fr (N. Wehr), ryerson1@llnl.gov (F. J. Ryerson)

Abstract. We carried out evaporation experiments on a B-type calcium–aluminium-rich inclusion (CAI) melt in a gas-mixing aerodynamic levitation laser furnace, at 1873 K and an oxygen partial pressure of $10^{-9.1}$ atm, for durations ranging from 60 to 600 s. Evaporation of SiO_2 and MgO follow the same trend as those observed in vacuum furnace experiments at the same temperature and starting composition, showing that their evaporation relative to one another from the melt is independent of pressure, oxygen fugacity, and hydrodynamical regime specific to the furnace. Isotopic ratios of Mg and Si in evaporation residues are used to derive fractionation factors of $\alpha^{26/24}\text{Mg}_{\text{vap-liqu}} = 0.9906 \pm 0.0004$ and $\alpha^{30/28}\text{Si}_{\text{vap-liqu}} = 0.9943 \pm 0.0003$, which are both significantly closer to unity than those found for evaporation in a vacuum, which translates to less isotope fractionation. The residues are also less isotopically fractionated than expected for cases in which transport of the gas species away from the melt is diffusion-controlled at 1-atm. By analysing the flow regimes in our furnace, we find that advection by the levitating gas is the primary mode of mass transport away from the melt surface, as opposed to diffusion-limited transport in a vacuum or 1-atm tube furnace. A modified Hertz–Knudsen–Langmuir formulation accounts for this process, and shows that isotopic fractionation of both Si and Mg reflect a saturation factor (ratio of the pressure of the evaporating species to vapour saturation pressure) equal to 0.75. This is in perfect accord with recent measurements of Cu isotopic fractionation using a similar furnace. The fact that three elements (Mg, Si, Cu) with varying equilibrium vapour pressures, activity coefficients in the liquid, and diffusion coefficients in the gas have the same scaling behaviour to saturation pressure is a strong indication that the mechanism controlling evaporation is driven by the hydrodynamical regime imposed in the furnace. Therefore, this class of experiments can be used to constrain processes in which advection dominates over

* Corresponding author.

diffusion, such as (but not limited to) planetary ejecta, tektites, giant impacts, nebular condensation in a turbulent flow, or nuclear fallout material. Finally, the possibility to reach high temperatures (in excess of 3500 K) in this furnace allows it to be used to evaluate the activity coefficients of melt components in extreme conditions relevant to molten planetary interiors (i.e., magma oceans), with a specific focus on refractory elements.

Keywords. Elemental fractionation, Isotopic fractionation, Aerodynamic levitation, Laser furnace, Extreme conditions, Planetary evaporation.

Manuscript submitted at the invitation of the editorial committee.

Manuscript received 9th March 2021, revised 21st April 2021, accepted 23rd April 2021.

1. Introduction

The chemical and isotopic effects of evaporation from molten silicates, and their cosmochemical consequences, have been widely studied under nebular conditions [Davis *et al.*, 1990, Hashimoto, 1990, Tissandier *et al.*, 2002, Tsuchiyama *et al.*, 1999, Yu *et al.*, 2003]. Under these conditions where the total gas pressure is extremely low ($<10^{-4}$ bar), vacuum or near-vacuum evaporation experiments are pertinent, because the conditions are applicable to numerous cosmochemical processes taking place in the early stages of the evolution of the solar nebula [Mendybaev *et al.*, 2021, Richter *et al.*, 2002].

As planetary accretion proceeds and primitive condensates agglomerate to form larger bodies, gravity enables them to retain an atmosphere [Massol *et al.*, 2016], whether captured from the nebula [Olson and Sharp, 2019] or more likely generated by the molten body's (magma ocean) evaporation itself [Young *et al.*, 2019]. The evaporation rate of a species i from a spherical surface of radius r is quantitatively described by the Hertz–Knudsen–Langmuir (HKL) equation,

$$\left(\frac{dn_i}{dt}\right)_{\text{net}} = -4\pi r^2 \frac{(p_{i,\text{eq}} - p_i)}{\sqrt{2\pi R M_i T}} \quad (1)$$

where R is the gas constant, M_i the molar mass of the gas species and T the temperature. Equation (1) shows that the evaporation rate depends on the difference between the equilibrium vapour pressure $p_{i,\text{eq}}$ and the actual partial pressure at the surface p_i . In planetary environments, free evaporation (e.g., when p_i tends to 0 and the evaporation rate is maximal) is obstructed by the evaporating species building up in the vapour surrounding the melt surface, and evaporation is influenced by the rate of chemical diffusion of the evaporated species away from the surface [Benedikt *et al.*, 2020, Young *et al.*, 2019]. As

gas pressure around the evaporating melt increases, equilibrium begins to predominate over kinetic effects (i.e., p_i approaches $p_{i,\text{eq}}$) to produce less net isotopic fractionation for a given degree of elemental evaporation, providing a pathway to decouple the elemental and isotopic effects of evaporation. However, advection of the surrounding gas can also alter evaporation rates by stripping away the boundary layer and partially nullifying the effect of chemical diffusion in the gas. This process is relevant to settings such as Moon formation [Charnoz *et al.*, 2021], tektite formation [Macris *et al.*, 2018, Moynier *et al.*, 2010], evaporation in the aftermath of a giant impact [Schlichting *et al.*, 2015] or during highly energetic events [Day *et al.*, 2020, Wimpenny *et al.*, 2020, 2019], or evaporation in the presence of supersonic winds as recently reported for the Moon [Saxena *et al.*, 2017], or molten rocky exoplanets [Nguyen *et al.*, 2020, Jackson *et al.*, 2010]. To investigate this process, we performed an experimental study of evaporation in a highly advective hydrodynamical regime, using an aerodynamic levitation laser-heated (ALLF) furnace (Figure 1). We measured elemental and isotopic evaporation of Si and Mg from a B-type CAI melt that has already been studied under vacuum conditions [Knight *et al.*, 2009, Richter *et al.*, 2007]. Our strategy was to use the same melt composition and temperature conditions as the previous experiments to isolate the effects resulting from the novel hydrodynamical regime particular to the ALLF.

2. Experimental setup

The ALLF is a contactless furnace where samples are heated and melted by an infrared CO₂ laser, and float in a conical nozzle where they are supported by a gas stream flowing vertically (upwards) from underneath, so as to counteract gravity [Hennet *et al.*,

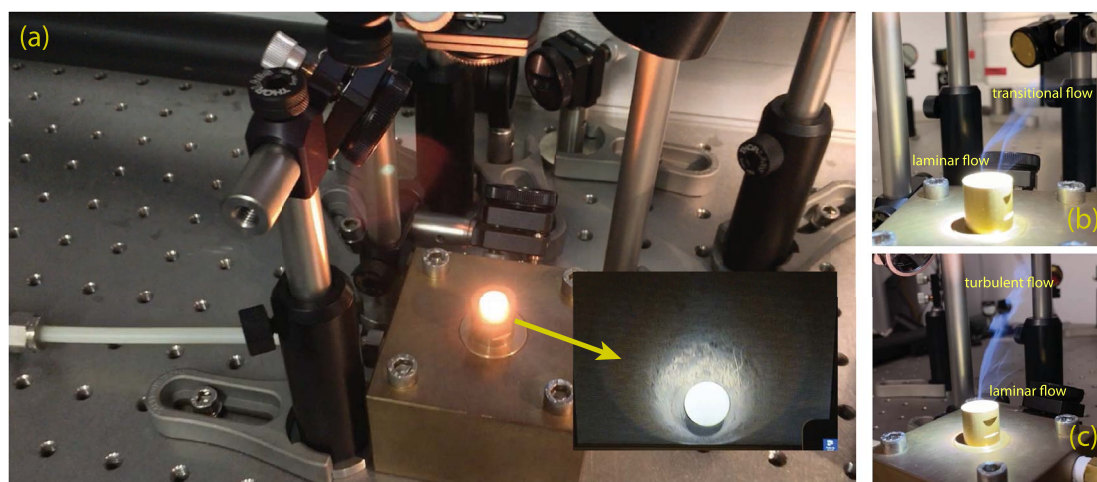


Figure 1. (a) Detailed view of the conical nozzle in the custom-built gas-mixing aerodynamic levitation laser furnace (ALLF) at IPGP (Paris, France) used in these experiments. The inset is a closeup view inside the nozzle, showing the molten spherical sample levitating in the gas stream. (b) and (c) Imaging of the evaporative (SiO and Mg gases) trail mimics that of a burning incense stick; the gas stream starts laminar around the sample inside the nozzle, and turns turbulent as it lifts away, due to the increasing Reynolds number.

2011]. Gas compositions can be changed by mixing (using multiple gas flow controllers) H₂, CO₂, and Ar gases, so as to allow variation in the oxygen fugacity of the surrounding gas. Some key advantages of this furnace are (i) the capability to perform contactless melting experiments, eliminating contamination from container materials, (ii) the production of homogeneous glassy samples resulting from a combination of ultrafast quenching rates (on the order of 1000 °C/s) and the absence of nucleation sites for crystals in a levitating spherical sample, and (iii) the ability to reach very high temperatures, in excess of 3000 °C (Figure 2).

The high velocity of the gas stream that levitates the sample gives rise to an advective hydrodynamical regime relative to the ones found in vacuum and 1-atm furnaces. In our experiments, the gas flow is in the range of 800–1000 sccm (14–18 cm³/s) through a 1.5 mm diameter hole in the nozzle, yielding an advective velocity on the order of 8–10 m/s. These values of gas advection provide the force to counter gravity and levitate the sample; stable levitation is achieved when the upwards drag force of the gas on the spherical sample exactly counters the downwards gravitational pull, $F_{\text{drag}} = F_{\text{grav}}$. For a gas with specific

mass ρ_{gas} at a velocity U , the force on a sphere of radius r is $F_{\text{drag}} = C_x((1/2)\rho_{\text{gas}}U^2)\pi r^2$ where C_x is the drag coefficient. The gravitational force on a melt of density ρ_{melt} and radius r is $F_{\text{grav}} = ((4/3)\pi r^3)\rho_{\text{melt}}g$, where $g = 9.8 \text{ m/s}^2$ is Earth's gravity. Therefore, when stable levitation is achieved the gas velocity is given by:

$$U_{\text{levitation}} = \left(\frac{8}{3C_x} \frac{\rho_{\text{melt}}}{\rho_{\text{gas}}} r g \right)^{\frac{1}{2}}. \quad (2)$$

Assuming an ideal drag coefficient for a sphere (0.47), a gas (argon) density of 1.7 kg/m³ and a melt (B-type CAI) density of 2800 kg/m³, and a sample radius of 1 mm (typical sample size), we find $U_{\text{levitation}} = 9.5 \text{ m/s}$ is consistent with the range of flow rates used. Note that the drag coefficient is a function of the Reynolds number, but changes very little in the range relevant for this furnace.

The Reynolds number characterising the flow around a sphere is:

$$Re = \frac{UL\rho_{\text{gas}}}{\eta} = \frac{UL}{\nu} \quad (3)$$

where L is the characteristic length of the flow (e.g., diameter of the sample in this case), η is the gas'

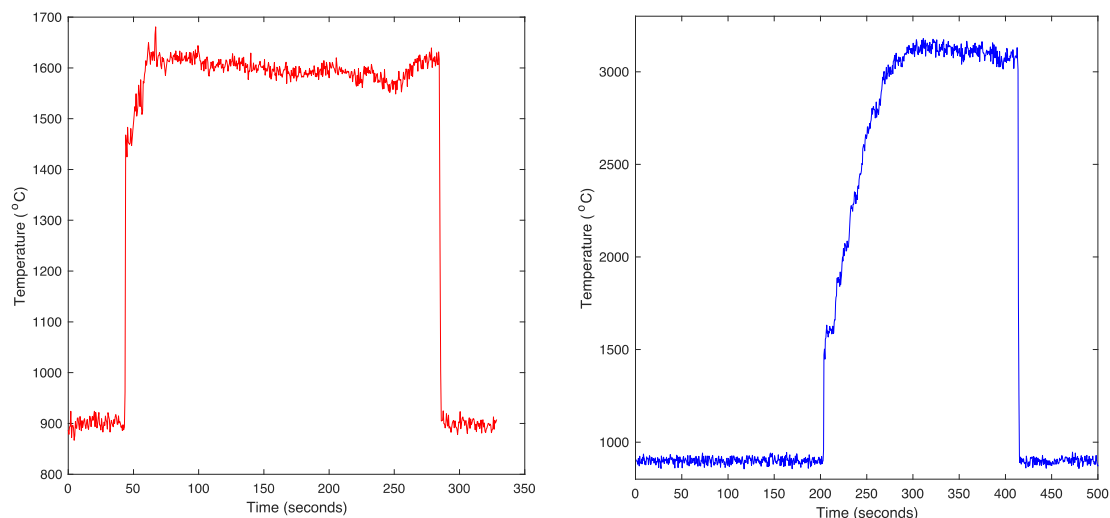


Figure 2. (Left) Typical heating runs (temperature versus time) of samples produced for this paper (shown here is that of sample VP4, Table 1). Note that the pyrometer only measures temperatures above 900 °C, and returns a baseline of 900 °C below that. (Right) The same starting composition, stably heated to 3100 °C for over 120 s demonstrating the temperature capability of the furnace.

dynamic viscosity, and $\nu = \eta/\rho$ its kinematic viscosity. Argon at room temperature has a kinematic viscosity $\nu = \eta/\rho = 1.4 \times 10^{-5} \text{ m}^2/\text{s}$ and yields Re in the range $\sim 1000\text{--}1500$, which corresponds to a transitional regime between laminar and turbulent flows. However, at high gas temperature in the vicinity of the sample, kinematic viscosity increases to $8 \times 10^{-5} \text{ m}^2/\text{s}$ (value at 1600 °C) to yield a Re in the 200–300 range. The flow at this scale is expected to be laminar, which is confirmed by imaging of the “smoke” trail of the evaporating sample in Figures 1(b) and (c); the flow in the nozzle around the sample is laminar, and transitions towards turbulence in the far field as Re increases (due to the combined effects of increasing L and decreasing ν), akin to smoke coming out of an incense stick.

The relative magnitude of the two transport mechanisms, chemical diffusion and advection, in stripping the evaporating species away from the evaporation surface can be evaluated by the nondimensional Péclet (Pe) number (dimensionless ratio of advection/diffusion), which is the product of the Reynolds number (Re , inertia/viscosity) and the Schmidt (Sc ,

viscosity/diffusion) number:

$$Sc = \frac{\eta}{D\rho_{\text{gas}}} \quad (4)$$

$$Pe = \frac{\text{advection}}{\text{diffusion}} = Re Sc = \frac{UL}{D} \quad (5)$$

where D is the diffusion coefficient of the evaporating species in the surrounding gas (on the order of $10^{-4} \text{ m}^2/\text{s}$). In the levitation furnace, Pe is on the order of 10, whereas it drops to 0.1 in the tube furnace (gas flows Sossi *et al.*, 2019, 2020 on the order of 0.1 m/s) and essentially to 0 in a vacuum furnace, highlighting advection as the principal mechanism for mass transport in our experiments compared to those performed in traditional furnaces where the only mode of mass transport away from the sample is due to chemical diffusion of the evaporate in a self-generated compositional gradient.

These terms are combined in the Sherwood number (Sh), which is the ratio of mass transfer by convection to diffusion (the mass transfer equivalent of the Nusselt number for heat), and is defined as:

$$Sh = \frac{k_c r}{D} \quad (6)$$

where k_c is the mass transfer coefficient, and can

Table 1. Elemental and isotopic composition of the evaporated samples from this study (top) in the levitation furnace, along with the elemental data from evaporated samples in a vacuum furnace [Richter *et al.*, 2007] carried out on the same starting melt composition (B-type CAI) and at the same temperature (1873 K)

Sample	This study															
	MgO (wt%)	SiO ₂ (wt%)	Al ₂ O ₃ (wt%)	CaO (wt%)	MgO/Al ₂ O ₃	SiO ₂ /Al ₂ O ₃	<i>f</i> (Mg)	<i>f</i> (Si)	d26Mg- BHVO-2G ‰	2se ‰	d25Mg- BHVO-2G ‰	2se ‰	d30Si- BHVO-2G ‰	2se ‰	d29Si- BHVO-2G ‰	2se ‰
Starting	12	46	19	23	0.6316	2.4211										
VP1	11.61	37.62	22.99	27.78	0.5050	1.6364	0.800	0.676	-3.78	0.19	-1.98	0.12	-1.73	0.04	-0.78	0.02
VP2	12.05	40.03	21.74	26.18	0.5543	1.8413	0.878	0.761	-4.39	0.21	-2.29	0.12	-2.63	0.17	-1.27	0.08
VP3	11.9	41.45	21.16	25.49	0.5624	1.9589	0.890	0.809	-4.80	0.22	-2.49	0.14	-2.68	0.31	-1.17	0.30
VP4	11.94	41.68	21.08	25.31	0.5664	1.9772	0.897	0.817	-4.62	0.22	-2.40	0.13	-2.79	0.07	-1.33	0.05
VP5	11.9	39.08	22.25	26.77	0.5348	1.7564	0.847	0.725	-4.22	0.28	-2.19	0.15	-2.26	0.28	-0.97	0.26
VP6	10.77	34.81	24.51	29.92	0.4394	1.4202	0.696	0.587	-2.27	0.14	-1.15	0.10	-1.04	0.11	-0.40	0.06
Richter <i>et al.</i> [2007]																
Sample	MgO (wt%)	SiO ₂ (wt%)	Al ₂ O ₃ (wt%)	CaO (wt%)	MgO/Al ₂ O ₃	SiO ₂ /Al ₂ O ₃										
R2-13	4.55	29.40	30.21	35.84	0.1506	0.9732										
R2-15	5.24	30.16	29.53	35.11	0.1774	1.0213										
R2-14	0.04	20.86	36.10	43.00	0.0011	0.5778										
R2-9	0.02	16.29	39.28	44.41	0.0005	0.4147										
R2-8	0.03	8.54	45.21	46.22	0.0007	0.1889										
R3-2	12.22	46.36	19.31	22.11	0.6328	2.4008										
R3-1	9.62	33.93	26.24	30.21	0.3666	1.2931										
R3-20	6.43	31.01	29.11	33.45	0.2209	1.0653										
R3-21	9.44	33.69	26.32	30.54	0.3587	1.2800										
R3-4	4.60	30.84	30.20	34.36	0.1523	1.0212										
R3-7	0.20	22.40	36.01	41.39	0.0056	0.6220										
R3-19	6.70	31.34	28.86	33.11	0.2322	1.0859										
R3-18	4.34	29.39	30.81	35.46	0.1409	0.9539										
R3-8	1.65	26.73	33.21	38.40	0.0497	0.8049										
R3-5	0.12	17.74	38.36	43.78	0.0031	0.4625										

be described by the Frössling correlation [Frössling, 1938] as:

$$Sh = 2 + 0.552Re^{\frac{1}{2}} Sc^{\frac{1}{3}} = 2 + 0.522Pe^{\frac{1}{2}} Sc^{-\frac{1}{6}} \quad (7)$$

which, with *Sc* on the order of 0.05 for our experiments, is valid for *Re* up to ~1000. Equation (7) therefore illustrates that higher values of *Pe* increase mass transfer (*k_c*) around the sample thereby effectively decreasing the surface pressure.

3. Experiments and analyses

A B-type CAI composition (Table 1) powder mix (identical to the one used in Knight *et al.* [2009] and Richter *et al.* [2007]) was made by mixing and milling high purity powders (SiO₂, MgO, Al₂O₃, CaCO₃), firing them at 900 °C overnight, and pressing them to

a pellet. At first, six 15-mg chunks of the pellet were loaded in the conical nozzle of the ALLE, and fused at 1600 °C using pure O₂ levitating gas for 30 s, to ensure full melting and homogenisation. Oxygen was used in this preliminary step so as to minimise the evaporation of Si and Mg, which have a very low evaporation rate at that temperature in an oxidising gas [Sossi *et al.*, 2019]. The samples were then rapidly quenched to spherical glass samples (~2 mm diameter) with a cooling rate of 850 °C/s. These six identical samples were then fused a second time at 1600 °C, using an Ar–CO₂–H₂ gas mixture, with a fixed molar ratio of 92% Ar, 1.6% CO₂, and 6.4% H₂. At 1873 K, the oxygen fugacity of that mixture is log *f*O₂ = -9.1, corresponding to 0.5 log unit below the iron–wüstite buffer (log *f*O₂ = -8.6). The samples were evaporated for durations varying between 180 and 900 s,

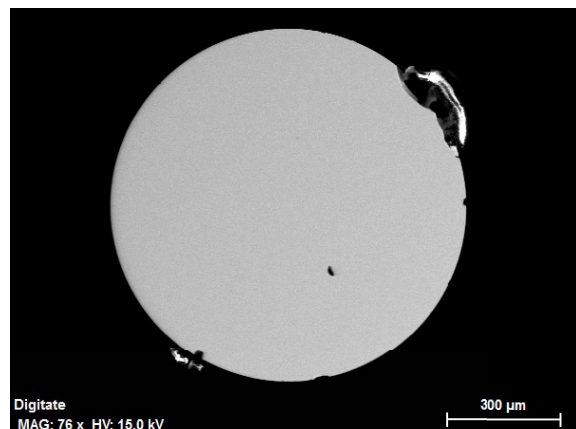


Figure 3. Back-scattered SEM image of run VP6; the spherical sample was cut in half and polished on the flat (equatorial) side prior to being imaged and compositionally analysed on the SEM.

with a typical thermal history shown in Figure 2. The samples were once again rapidly quenched to glass by shutting down laser power.

The samples were then cut in two halves using a diamond saw, mounted in epoxy, diamond-polished on the flat (equatorial) side, and imaged and chemically analysed using a Zeiss Auriga 40 field-emission gun scanning electron microscope (SEM) equipped with a windowless Bruker Quantax XFlash EDX detector. Inspection using back-scattered electron imaging (Figure 3) confirmed that the samples were glassy and homogeneous at all scales, with no sign of crystal nucleation. Quantitative elemental analyses were performed by standardised EDX using the K-lines of Mg, Si, Ca, and Al (which with oxygen, are the only elements in our synthetic sample); large window scans, line scans, and point analyses again confirmed chemical homogeneity at all scales (millimetric to sub-micron). The compositions of the six evaporated samples are reported in Table 1.

The Mg and Si isotopic compositions of the evaporated glasses were measured [Deng *et al.*, 2021] by laser ablation multi-collector inductively-coupled-plasma mass spectrometry (MC-ICP-MS) combining a 193-nm ultra-short ATLEX 300si excimer laser system with a Thermo-Scientific NeptunePlus at IPGP (Paris, France). To monitor matrix-induced Mg and Si isotopic effects, four CaO–Al₂O₃–MgO–SiO₂ (CMAS)

glasses were synthesised from the starting powders of the evaporation experiments, and were analysed along with the evaporated glasses and two other glasses (BCR-2G and TB-1G). To correct for instrumental fractionation, a basaltic glass BHVO-2G was analysed after every three or four analyses of the samples. The measurements were carried out with an ablation spot size of 110 μm, a repetition rate of 4 Hz and a He gas flow rate of 1.2 L/min. The typical laser fluence was 4.05 J/cm², and each ablation spot contained 400 laser burst shots. The washout time was 10 s after the end of ablation, and the pause time after each ablation spot was 60 s. The mass spectrometer was operated in medium mass resolution mode ($M/\Delta M \approx 5000$), which is sufficient to resolve the major isobaric interferences from ¹²C¹⁴N⁺ on ²⁶Mg⁺, and from ¹⁴N¹⁶O⁺ on ³⁰Si⁺. For Mg isotopes, the measurements were conducted on the lower masses of the ²⁴Mg⁺ (L3-F), ²⁵Mg⁺ (C-F) and ²⁶Mg⁺ (H2-F) peaks to avoid ¹²C¹⁴N⁺. As this cup configuration and resolution cannot prevent the interference of ⁴⁸Ca²⁺ on ²⁴Mg⁺, the central mass was moved from 25 to 23 a.m.u. to simultaneously measure the intensities of ⁴⁴Ca²⁺ (mass 22, L4-F) and ²⁴Mg⁺ (mass 24, H2-F), which were used afterwards to correct for the ⁴⁸Ca²⁺ interferences. Since all the analysed materials are terrestrial, mass-independent effects on the raw Mg isotopic ratios can only arise from ⁴⁸Ca²⁺ interferences on ²⁴Mg⁺. This allows for precise determination of the instrumental ⁴⁴Ca²⁺/⁴⁸Ca²⁺ ratio (10.25 ± 0.37) and thus a reliable correction of ⁴⁸Ca²⁺ interferences. For Si isotopes, the measurements were carried out on the lower masses of ²⁸Si⁺ (L3-F), ²⁹Si⁺ (C-F) and ³⁰Si⁺ (H3-F) peaks to avoid ¹⁴N¹⁶O⁺ interferences. Using these instrumental settings, each laser ablation spot measurement consists of 13 cycles with an integration time of 4 s per cycle for Mg isotope analyses, whereas 21 cycles with the same integration time were used for Si isotope measurements. Data reduction was carried out by integrating these cycles excluding the transient cycles with intensity varying more than 25% from the plateau intensity at the start or the end of ablation. The background subtraction was conducted after a polynomial fit to the background cycles before ablation. The Mg and Si isotopic data of the evaporated glasses and the other glasses are given in Table 1, in per mil notation (‰) relative to the bracketing standard BHVO-2G.

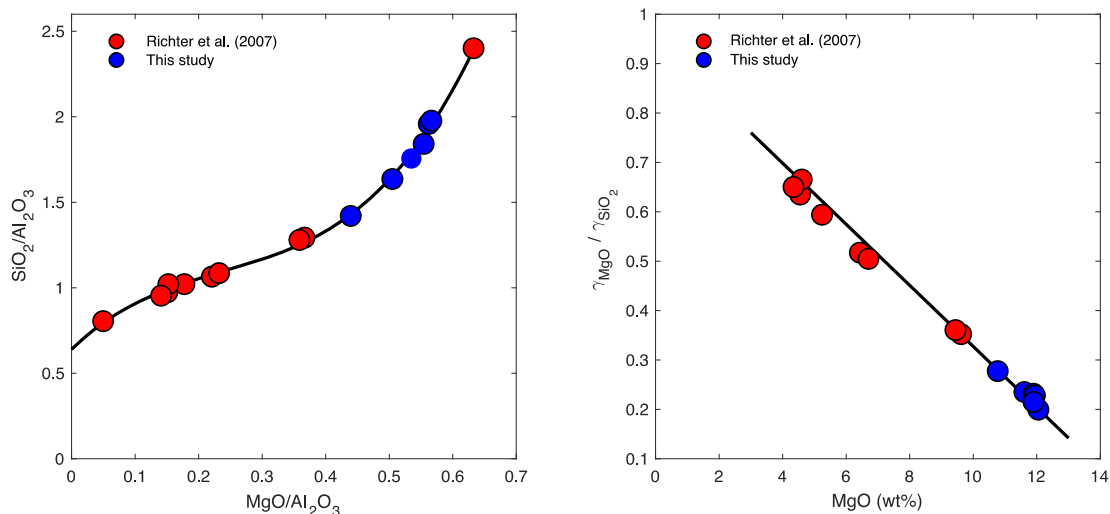


Figure 4. (Left) Compositional evolution of the evaporating melt (Si and Mg). Our data (blue circles) were plotted alongside the data (red circles) from Richter et al. [2007] that were gathered on the same melt composition and at the same temperature, albeit in a different evaporative regime (vacuum evaporation versus 1-atm evaporation in an advective flow). The path is identical, and the black curve fitting the evaporative path was fitted only to the Richter et al. [2007] data, illustrating the remarkable agreement with our data. This is expected, due to the fact that MgO and SiO₂ evaporation have the same dependence on the composition of surrounding gas (i.e. f_{O_2}), see main text. The uncertainties on the analytical data are on the order of symbol size. (Right) The ratio of activity coefficients of evaporating components (MgO and SiO₂) in the melt, plotted as a function of residual melt composition.

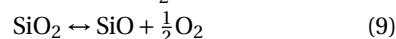
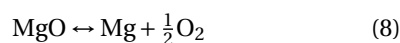
4. Results and discussion

4.1. Elemental fractionation

The chemical homogeneity of Mg and Si observed for all samples indicates that diffusion of these elements through the melt to the surface did not inhibit their ability to evaporate. The elemental composition (MgO and SiO₂) of the evaporated samples is plotted in Figure 4, alongside those from the study of Richter et al. [2007] which were performed on the same melt composition and at the same temperature, but under vacuum conditions (i.e. in a diffusive evaporative regime versus an advective evaporative regime for the levitation runs). This shows that the compositional evolution follows the same path, regardless of the difference in pressure and therefore evaporation regime. Both MgO and SiO₂ concentrations are normalised to Al₂O₃ concentration, a component that does not readily evaporate, so as to correctly describe their evaporation from the melt. The standard method consists of plotting MgO and SiO₂ mass loss, which requires measurement of the total

mass of the glass samples, both before and after evaporation. With masses in the 10-mg range and mass losses in the sub-mg range, the uncertainties on these measurements are so large, if at all resolvable, that they disqualify the use of this method.

The noteworthy consistency of the evaporation trends observed in vacuum experiments and those presented herein is due to the fact that both Mg and Si evaporate with the same change in speciation between liquid and vapour phase (i.e., two electrons are exchanged). Therefore their relative partial pressures are independent of that of oxygen (f_{O_2}) around them. This is best expressed by the equilibrium constants of the evaporation reactions; with Mg and SiO the dominant gas species at the (P, T, f_{O_2}) conditions of the experiments, the evaporation reactions of MgO and SiO₂ from the melt are (liquid species on the left, gas species on the right):



with equilibrium constants given by:

$$K_{\text{Mg}} = \frac{p(\text{Mg})}{X_{\text{MgO}} \cdot \gamma_{\text{MgO}}} \cdot (f\text{O}_2)^{\frac{1}{2}} \quad (10)$$

$$K_{\text{Si}} = \frac{p(\text{SiO})}{X_{\text{SiO}_2} \cdot \gamma_{\text{SiO}_2}} \cdot (f\text{O}_2)^{\frac{1}{2}} \quad (11)$$

where X_i are the molar fractions and γ_i the activity coefficient of component i in the melt, $f\text{O}_2$ the partial pressure of oxygen in the gas, and $p(i)$ the pressure of the evaporating species i in the gas.

The residual silicon and magnesium content of the melt can be obtained by integrating the evaporation flux (Equation (1)) over time [Sossi *et al.*, 2020], and is given by:

$$\frac{\text{Si}(t)}{\text{Si}(0)} = \exp\left(-\alpha_{\text{ec}} \frac{\gamma_{\text{SiO}_2} K_{\text{Si}} 3V_{\text{mol}}}{(f\text{O}_2)^{\frac{1}{2}} r} \times \left(\frac{1}{2\pi M_{\text{SiO}} RT}\right)^{\frac{1}{2}} \cdot t\right) \quad (12)$$

$$\frac{\text{Mg}(t)}{\text{Mg}(0)} = \exp\left(-\alpha_{\text{ec}} \frac{\gamma_{\text{MgO}} \cdot K_{\text{Mg}} 3V_{\text{mol}}}{(f\text{O}_2)^{\frac{1}{2}} r} \times \left(\frac{1}{2\pi M_{\text{Mg}} RT}\right)^{\frac{1}{2}} \cdot t\right) \quad (13)$$

where t is evaporation time, T temperature, α_{ec} the evaporation constant, r the radius of the melt sample, V_{mol} its molar volume, and M_i the molar mass of the evaporating species i in the gas. Note that Si and Mg on the left-hand side of the equations are not the molar concentrations (X_i) of SiO_2 and MgO in the melt but their actual total content, because the HKL equation is a mass balance equation.

In principle, the evaporation constant α_{ec} could be different for MgO and SiO_2 , and has indeed been shown to vary if evaporation were to take place from the solid state (such as from forsterite, e.g., [Wang *et al.*, 1999]); but experiments and theory have shown that α_{ec} during evaporation from liquids is indistinguishable from unity (see [Burns, 1966, Shornikov, 2015, Sossi *et al.*, 2019], and references therein). Integrating the HKL equation to yield (12) and (13) assumes that all the terms inside the exponential are constant during evaporation. This is not formally true for activity coefficients and molar volume which depend on composition, nor for sample radii that decrease with evaporation. Using the integrated equations as shown here assumes that any changes occurring during evaporation are sufficiently smooth

or vary slowly enough to justify brute-force integration. This is clearly the case during evaporation of minor components or trace elements for which the equation was developed [Sossi *et al.*, 2019], but we stress that these equations should be used with great caution when considering the evaporation of major components in the melt.

The relative depletion (by evaporation) of Si and Mg from the sample is then described by the ratio:

$$\frac{\ln \frac{\text{Si}(t)}{\text{Si}(0)}}{\ln \frac{\text{Mg}(t)}{\text{Mg}(0)}} = \frac{\gamma_{\text{SiO}_2} K_{\text{Si}}}{\gamma_{\text{MgO}} K_{\text{Mg}}} \cdot \left(\frac{M_{\text{Mg}}}{M_{\text{SiO}}} \right)^{\frac{1}{2}} \quad (14)$$

which is independent of gas pressure (and oxygen fugacity in particular) surrounding the sample and only depends on temperature (K) and the activity coefficient (γ), which may vary with melt composition.

Note that (14) is only formally correct in the ideal case where the evaporating species does not interact with the melt and is instantly removed from the surface (i.e. kinetic theory). In a realistic system, a gaseous boundary layer builds up around the sample, limiting the evaporating flux by chemical diffusion. This introduces a scaling factor to (Equations (12)–(14)), a function of the pressure saturation factor [Sossi *et al.*, 2020, Young *et al.*, 2019], and (14) becomes:

$$\frac{\ln \frac{\text{Si}(t)}{\text{Si}(0)}}{\ln \frac{\text{Mg}(t)}{\text{Mg}(0)}} = \frac{\gamma_{\text{SiO}_2} \cdot K_{\text{Si}}}{\gamma_{\text{MgO}} \cdot K_{\text{Mg}}} \cdot \left(\frac{M_{\text{Mg}}}{M_{\text{SiO}}} \right)^{\frac{1}{2}} \cdot \left(\frac{1 - \frac{p_{\text{SiO}}}{p_{\text{SiO,eq}}}}{1 - \frac{p_{\text{Mg}}}{p_{\text{Mg,eq}}}} \right) \quad (15)$$

where p_i is the actual pressure of evaporating species i in the gas, and $p_{i,\text{eq}}$ the pressure for that same species at liquid–gas equilibrium (i.e. vapour saturation pressure), and the ratio $p_i/p_{i,\text{eq}}$ is the pressure saturation factor. This realistically brings the evaporative flux to 0 in the limit where gas pressure reaches saturation pressure, and to the maximum value derived from the kinetic theory of gases (Equation (14)) when the evaporation species is instantly removed ($p_i \rightarrow 0$). The fact that the data (Figure 4) is perfectly reproduced by (14) is an indication that the last term in (15) is near or equal to unity (i.e., the ratio of the saturation factors of SiO and of Mg are ~ 1), which is confirmed subsequently by isotopic analysis.

Equation (14) (or (15)) can be inverted to express the activity coefficients of the components evaporating from the melt as a function of measurable parameters, hence allowing a direct measure of these activity coefficients in temperature ranges that are unreachable using standard furnaces. Equation (14) becomes:

$$\frac{\gamma_{\text{MgO}}}{\gamma_{\text{SiO}_2}} = \frac{\ln \frac{\text{Mg}(t)}{\text{Mg}(0)}}{\ln \frac{\text{Si}(t)}{\text{Si}(0)}} \cdot \frac{K_{\text{Si}}}{K_{\text{Mg}}} \cdot \left(\frac{M_{\text{Mg}}}{M_{\text{SiO}}} \right)^{\frac{1}{2}} \quad (16)$$

and the left-hand term can be evaluated directly from the experiments (Si and Mg content) and using

thermodynamic data to evaluate the equilibrium constants K of evaporation reactions (10) and (11). Using the JANAF [Chase, 1998] tables, we find the following Gibbs free energies of reaction (in kJ/mol) of the evaporative species (Mg and SiO) from their melt components MgO and SiO₂: $\Delta_f G_{\text{MgO-Mg}} = 635.05 - 0.171 T$, and $\Delta_f G_{\text{SiO}_2\text{-SiO}} = 759.72 - 0.232 T$, allowing computation of the relevant equilibrium constants using $K = \exp(-(\Delta_f G/RT))$. The ratio of the activity coefficients (Equation (16)) is plotted in Figure 4. Once again, we note a remarkable agreement (or rather continuity) between vacuum furnace experiments and our levitation furnace experiments. The ratio $\gamma_{\text{MgO}}/\gamma_{\text{SiO}_2}$ increases during evaporation as MgO concentration drops (i.e., as evaporation proceeds), explaining the observed preferential MgO evaporation compared to SiO₂. This behaviour was identified by Richter *et al.* [2007] and modelled by Alexander [2002] using the MELTS algorithm of [Ghiorso *et al.*, 2002, Ghiorso and Sack, 1995] and found values near ~ 0.2 for similar compositions. That independent thermodynamic estimates of activity coefficients are similar to those calculated experimentally, assuming evaporation coefficients are unity, provides *post hoc* evidence for such an assumption. We note that the activity coefficient ratios determined here are integrated mean values over the evaporation duration. This consideration is important because the activity coefficients of Mg and Si, as major components, change as evaporation proceeds and the bulk composition of the melt evolves.

4.2. Isotopic fractionation

Isotopic analysis (Si and Mg isotopes) of the samples show that they are fractionated, following a mass-dependent fractionation law, as seen on three-isotope plots (Figure 5). Our experimentally derived slope for magnesium ($\delta^{25}\text{Mg}-\delta^{26}\text{Mg}$) is 0.531 ± 0.006 and that for silicon ($\delta^{29}\text{Si}-\delta^{30}\text{Si}$) is 0.522 ± 0.16 . These values are consistent, within uncertainties, with the theoretically expected slopes for equilibrium and kinetic fractionation lines [Young *et al.*, 2002], given by $((1/m_1) - (1/m_2))/((1/m_1) - (1/m_3))$ and $(\ln m_1 - \ln m_2)/(\ln m_1 - \ln m_3)$, respectively. With Mg being the predominant gas species for magnesium evaporation, the theoretical equilibrium slope is 0.520 and the theoretical kinetic slope is 0.510. For silicon, with SiO as the predominant gas species, the

theoretical equilibrium slope is 0.511 and the theoretical kinetic slope is 0.506.

Accurate isotopic fractionation factors (α) from our experimental runs can be obtained directly by comparing the isotopic fractionation to the evaporative loss f of each element (i.e. $\text{Si}/\text{Si}_{\text{initial}}$ and $\text{Mg}/\text{Mg}_{\text{initial}}$), which are reported in Table 1. Our data for Mg and Si is plotted in Figure 6, and shows a linear dependence on $\ln f$ (Rayleigh fractionation) defined by:

$$\ln\left(\frac{R}{R_0}\right) = (1 - \alpha) \ln f \quad (17)$$

where R is the isotopic ratio ($^{25}\text{Mg}/^{24}\text{Mg}$, $^{26}\text{Mg}/^{24}\text{Mg}$, $^{29}\text{Si}/^{28}\text{Si}$, $^{30}\text{Si}/^{28}\text{Si}$) in the evaporated sample normalised to that of a standard (here, the BHVO-2G standard), and R_0 that same ratio in an unevaporated sample. Since samples produced in the levitation furnace are always evaporated to some extent, Equation (17) can be rewritten as:

$$\ln R = (1 - \alpha) \ln f + \ln R_0 \quad (18)$$

where the last term is a constant related to the isotopic difference between the samples' starting material and the standard used. Because this only adds an arbitrary intercept to the Rayleigh equation (Equation (17)), it does not affect the slope, which is the essential parameter we are seeking to determine. All data plotted in Figure 6 is corrected for that intercept value, to make the figure more readable and more consistent with a traditional Rayleigh plot, with all fits going through the origin.

Firstly, we verify that for each element, the ratio of slopes (1-a) of the lighter versus heavier isotope in Figure 6 is equal (within uncertainties) to the slope found in the 3-isotope plot (Figure 5).

The isotopic fractionation factors α observed in our experiments can be compared to those measured in purely kinetic (vacuum) evaporation experiments. The isotopic fractionation factors in our experiments are much higher (closer to unity), indicating less isotopic fractionation for an otherwise constant degree of elemental evaporation (Table 2). Our data can also be compared to those expected in a 1-atm tube furnace [Sossi *et al.*, 2020] in which diffusion through the gas phase is the limiting variable, and again, our isotopic fractionation factors are also closer to unity.

This important difference in isotopic fractionation factors between previous experiments (vacuum or 1 bar) and ours must be due to the fundamental difference in the mass transport mechanism involved. While chemical diffusion away from the sample (in a self-sustained chemical gradient) is the main mode of transport in vacuum or tube furnaces because the gas flow around the evaporating sample has $Pe < 1$, advective transport dominates in the levitation furnace where $Pe > 1$ as seen on its effect on the Sherwood number (Equation (7)). Empirically this change in mode of mass transport has a strong effect on isotopic fractionation, and we argue here it is the reason for our observation of isotopic fractionation factors that tend closer to unity than predicted. Indeed, in the limit where diffusion is overrun by advection, the difference in the diffusion constants of two evaporating isotopic species tends to vanish, and their effective values converge, e.g. their ratio (D_i/D_j) $\rightarrow 1$. In this case, the formalism of ideal isotopic fractionation in vacuum (purely kinetic) can be applied to the isotopic fractionation factors so that:

$$\alpha_{i,\text{net}} = 1 - \left(\left(\frac{M_j}{M_i} \right)^{\frac{1}{2}} - 1 \right) \left(1 - \frac{p_i}{p_{i,\text{eq}}} \right) \quad (19)$$

where $\alpha_{i,\text{net}}$, M_i , p_i and $p_{i,\text{eq}}$ are the observed (i.e. net) isotopic fractionation factor (Table 2), mass, pressure and vapour saturation pressure of evaporating species i , respectively, and M_j the mass of the reference species (24 for Mg, 44 for SiO). One can verify that this equation satisfies both limits, where the ideal value of $(M_j/M_i)^{1/2}$ is found in perfect vacuum (i.e. $p_i \rightarrow 0$) and where no fractionation ($\alpha_{i,\text{net}} = 1$) is observed for melt-vapour equilibrium at saturation (i.e. $p_i \rightarrow p_{i,\text{eq}}$). This formulation assumes that equilibrium isotopic fractionation between melt and gas is zero, which is reasonable considering the high temperature of the experiments and its $1/T^2$ dependence [Urey, 1947].

Because p_i and $p_{i,\text{eq}}$ cannot be measured, we considered the ratio $p_i/p_{i,\text{eq}}$ (the saturation factor) appearing in (19) as a variable that can be constrained from our data. For both $\delta^{26}\text{Mg}$ and $\delta^{25}\text{Mg}$ (with Mg as the gas species), we find $p_i/p_{i,\text{eq}} = 0.74 \pm 0.02$, a value indistinguishable from that obtained for both $\delta^{30}\text{Si}$ and $\delta^{29}\text{Si}$ (with SiO as the gas species) where $p_i/p_{i,\text{eq}} = 0.76 \pm 0.04$. It is noteworthy that this value of 0.74 ± 0.01 was found recently for Cu evaporation conducted in a levitation furnace [Ni *et al.*, 2021].

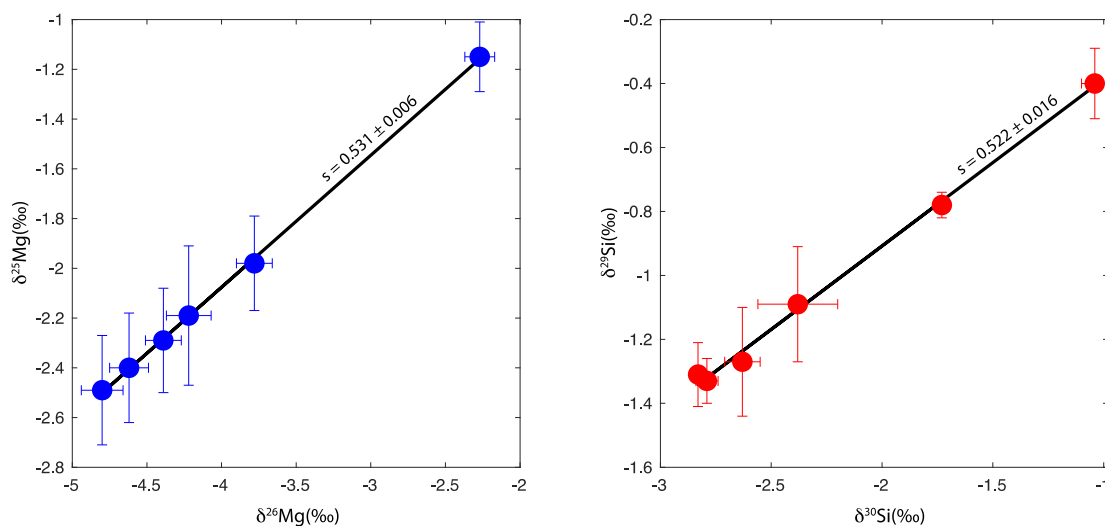


Figure 5. Isotopic composition of the evaporated samples shown in a three-isotope plot. Delta values are calculated with respect to the terrestrial BHVO-2G standard (Table 1). Both Mg (left) and Si (right) isotopes show quasi-perfect, straight lines consistent with mass-dependent isotopic fractionation. The slopes are consistent, within uncertainties, with theoretically calculated slopes for equilibrium and kinetic fractionation (see main text).

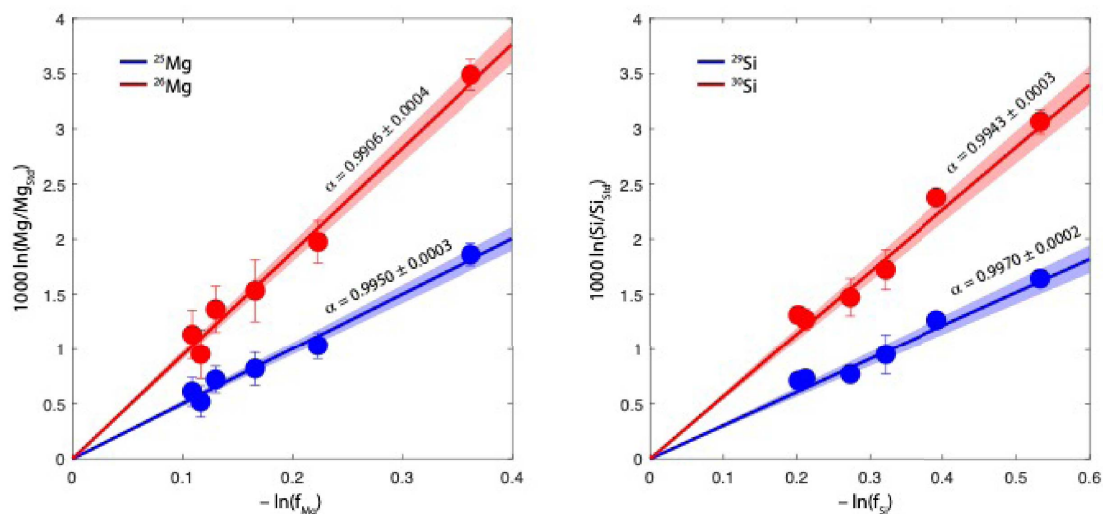


Figure 6. Isotopic composition of the evaporated samples as a function of evaporative loss. Magnesium is shown on the left and silicon on the right panels. The blue and red lines correspond to the lighter (^{25}Mg and ^{29}Si) and heavier (^{26}Mg and ^{30}Si) isotope, respectively. The standard to which all data is normalised is the terrestrial BHVO-2G standard. The log-log plot of the data shows a remarkable linear behaviour, fully consistent with a Rayleigh evaporation regime (i.e., distillation). The dashed area corresponds to the 1-sigma uncertainty in the fit, and α is the isotopic fractionation factor (Equation (17)) and is equal by definition to $(1 - \text{slope}/1000)$.

Table 2. Isotopic fractionation factors from this study in the levitation furnace, compared with those obtained on the same composition and at the same temperature in a vacuum furnace [Richter *et al.*, 2007], and to those expected at 1 bar for a diffusive transport mechanism recalculated from Sossi *et al.* [2020]

	Advective (this study)	2SD	Vacuum [Richter <i>et al.</i> , 2007]	1-atm [Sossi <i>et al.</i> , 2020]
$\delta^{30}\text{Si}$	0.9943	0.0006	0.9780	0.9933
$\delta^{29}\text{Si}$	0.9970	0.0004	0.9888	0.9966
$\delta^{26}\text{Mg}$	0.9906	0.0008	0.9608	0.9841
$\delta^{25}\text{Mg}$	0.9950	0.0006	0.9798	0.9918

The fact that the saturation factor is the same for Si, Mg, and Cu despite their differing evaporation rates from the melt and differing diffusion rates through the gas implies that this factor is controlled by a property common to all systems. We argue that this property is the effective pressure reduction due to increased mass transport in a flow with a high Sherwood number. While in principle this pressure reduction could be calculated from (7), we note that flows in which $Re > 200$ are inherently unstable (i.e., transitional) and require detailed hydrodynamic treatment to fully resolve [Michaelides, 2003], and hence cannot be applied in a quantitative manner in this work. It shows that advection is acting more quickly than the timescale for which a diffusive gradient can be established around the melt, and hence, the flow conditions around the sample are imposing a steady state transport rate.

5. Conclusions

These experiments demonstrate that the levitation furnace is an effective tool to study elemental and isotopic evaporation of silicate melts. Because this furnace is capable of reaching temperatures in excess of 3400 K, which are well beyond the limits of traditional (vacuum or tube) furnaces, it is well adapted to the study of the evaporation of refractory elements. Moreover, it would allow the measurement of activity coefficients of melt components at extreme temperatures (using (16)), and because the experiments are quick (on the order of minutes) and have a rapid turnover, could facilitate the gathering of large amounts of highly reproducible data to provide accurate measurements of these coefficients over a large range of previously unattainable temperatures.

Isotopic fractionation shows that the evaporation process here is controlled by advection instead of diffusion. Such a regime is relevant in certain astrophysical environments, and these experiments can help constrain evaporation processes occurring in such conditions [Macris *et al.*, 2018, Schlichting *et al.*, 2015, Saxena *et al.*, 2017, Nguyen *et al.*, 2020, Jackson *et al.*, 2010, Charnoz *et al.*, 2021]. The possibility of reaching a diffusive regime that is relevant to other planetary processes could be envisioned by increasing the evaporation rates so as to restore a diffusive boundary, either by working at higher temperature, or more effectively so by operating at lower oxygen fugacity to increase the net evaporating flux. With a square root dependence of the flux of Mg and Si on $f\text{O}_2$ (Equations (10)–(11)) and with the capability to scan ten orders of magnitude in $f\text{O}_2$, we can achieve in principle a five orders of magnitude change in the evaporation rate, which could eventually re-establish diffusive boundary condition, which remains to be tested by further experiments.

Acknowledgements

James Badro expresses his infinite gratitude to the Bourcart–Gentil Foundation of the French Academy of Science for their award, and to the editors of the proceedings of that noble society (Comptes Rendus Géosciences) for the invitation to contribute this work in recognition of this honour. Paolo A. Sossi thanks the SNSF through Ambizione Fellowship grant 180025. We thank Maylis Landeau, Sébastien Charnoz, Marc Chaussidon, and Frank Richter for invigorating and refreshing discussions. We acknowledge the financial support of the UnivEarthS labex program at the University of Paris (ANR-10-LABX-0023 and ANR-11-IDEX-0005-02).

This work was supported by IPGP multidisciplinary program PARI, and by Paris–IdF region SESAME grant no. 12015908.

References

- Alexander, C. (2002). Application of MELTS to kinetic evaporation models of FeO-bearing silicate melts. *Meteorit. Planet. Sci.*, 37, 245–256.
- Benedikt, M. R., Scherf, M., Lammer, H., Marcq, E., Odert, P., Leitzinger, M., and Erkaev, N. V. (2020). Escape of rock-forming volatile elements and noble gases from planetary embryos. *Icarus*, 347, article no. 113772.
- Burns, R. P. (1966). Systematics of the evaporation coefficient Al_2O_3 , Ga_2O_3 , In_2O_3 . *J. Chem. Phys.*, 44, 3307–3319.
- Charnoz, S., Sossi, P. A., Lee, Y.-N., Siebert, J., Hyodo, R., Allibert, L., Pignatale, F. C., Landeau, M., Oza, A. V., and Moynier, F. (2021). Tidal pull of the Earth strips the proto-Moon of its volatiles. *Icarus*, 364, article no. 114451.
- Chase, M. W. (1998). *NIST JANAF Thermochemical Tables*. American Institute of Physics, Washington, DC, 4th edition.
- Davis, A. M., Hashimoto, A., Clayton, R. N., and Mayeda, T. K. (1990). Isotope mass fractionation during evaporation of Mg_2SiO_4 . *Nature*, 347, 655–658.
- Day, J. M. D., Moynier, F., Sossi, P. A., Wang, K., Meshik, A. P., Pravdivtseva, O. V., and Pettit, D. R. (2020). Moderately volatile element behaviour at high temperature determined from nuclear detonation. *Geochem. Perspect. Lett.*, 13, 54–60.
- Deng, Z., Chaussidon, M., Ebel, D. S., Villeneuve, J., Moureau, J., and Moynier, F. (2021). Simultaneous determination of mass-dependent Mg isotopic variations and radiogenic ^{26}Mg by laser ablation-MC-ICP-MS and implications for the formation of chondrules. *Geochim. Cosmochim. Acta*, 299, 163–183.
- Frossling, N. (1938). Über die verdunstung fallender tropfen. *Gerlands Beitr. Geophys.*, 52, 170–216.
- Ghiorso, M. S., Hirschmann, M. M., Reiners, P. W., and Kress, V. C. (2002). The pMELTS: a revision of MELTS for improved calculation of phase relations and major element partitioning related to partial melting of the mantle to 3 GPa. *Geochem. Geophys. Geosyst.*, 3, 1–35.
- Ghiorso, M. S. and Sack, R. O. (1995). Chemical mass transfer in magmatic processes IV. A revised and internally consistent thermodynamic model for the interpolation and extrapolation of liquid–solid equilibria in magmatic systems at elevated temperatures and pressures. *Contrib. Mineral. Petrol.*, 119, 197–212.
- Hashimoto, A. (1990). Evaporation kinetics of forsterite and implications for the early solar nebula. *Nature*, 347, 53–55.
- Hennet, L., Cristiglio, V., Kozaily, J., et al. (2011). Aerodynamic levitation and laser heating. *Eur. Phys. J. Spec. Top.*, 196, 151–165.
- Jackson, B., Miller, N., Barnes, R., Raymond, S. N., Fortney, J. J., and Greenberg, R. (2010). The roles of tidal evolution and evaporative mass loss in the origin of CoRoT-7 b. *Mon. Not. R. Astron. Soc.*, 407, 910–922.
- Knight, K. B., Kita, N. T., Mendybaev, R. A., Richter, F. M., Davis, A. M., and Valley, J. W. (2009). Silicon isotopic fractionation of CAI-like vacuum evaporation residues. *Geochim. Cosmochim. Acta*, 73, 6390–6401.
- Macris, C. A., Asimow, P. D., Badro, J., Eiler, J. M., Zhang, Y., and Stolper, E. M. (2018). Seconds after impact: insights into the thermal history of impact ejecta from diffusion between lechatelierite and host glass in tektites and experiments. *Geochim. Cosmochim. Acta*, 241, 69–94.
- Massol, H., Hamano, K., Tian, F., et al. (2016). Formation and evolution of protoatmospheres. *Space Sci. Rev.*, 205, 153–211.
- Mendybaev, R. A., Kamibayashi, M., Teng, F.-Z., Savage, P. S., Georg, R. B., Richter, F. M., and Tachibana, S. (2021). Experiments quantifying elemental and isotopic fractionations during evaporation of CAI-like melts in low-pressure hydrogen and in vacuum: constraints on thermal processing of CAIs in the protoplanetary disk. *Geochim. Cosmochim. Acta*, 292, 557–576.
- Michaelides, E. E. (2003). Hydrodynamic force and heat/mass transfer from particles, bubbles, and drops—the Freeman scholar lecture. *J. Fluids Eng.-Trans. ASME*, 125, 209–238.
- Moynier, F., Koeberl, C., Beck, P., Jourdan, F., and Telouk, P. (2010). Isotopic fractionation of Cu in tektites. *Geochim. Cosmochim. Acta*, 74, 799–807.
- Nguyen, T. G., Cowan, N. B., Banerjee, A., and Moores,

- J. E. (2020). Modelling the atmosphere of lava planet K2-141b: implications for low- and high-resolution spectroscopy. *Mon. Not. R. Astron. Soc.*, 499, 4605–4612.
- Ni, P., Macris, C. A., Darling, E. A., and Shahar, A. (2021). Evaporation-induced copper isotope fractionation: insights from laser levitation experiments. *Geochim. Cosmochim. Acta*, 298, 131–148.
- Olson, P. L. and Sharp, Z. D. (2019). Nebular atmosphere to magma ocean: a model for volatile capture during Earth accretion. *Phys. Earth Planet. Inter.*, 294, article no. 106294.
- Richter, F. M., Davis, A. M., Ebel, D. S., and Hashimoto, A. (2002). Elemental and isotopic fractionation of Type B calcium-, aluminum-rich inclusions: experiments, theoretical considerations, and constraints on their thermal evolution. *Geochim. Cosmochim. Acta*, 66, 521–540.
- Richter, F. M., Janney, P. E., Mendybaev, R. A., Davis, A. M., and Wadhwa, M. (2007). Elemental and isotopic fractionation of Type B CAI-like liquids by evaporation. *Geochim. Cosmochim. Acta*, 71, 5544–5564.
- Saxena, P., Elkins-Tanton, L., Petro, N., and Mandell, A. (2017). A model of the primordial lunar atmosphere. *Earth Planet. Sci. Lett.*, 474, 198–205.
- Schlichting, H. E., Sari, R., and Yalinewich, A. (2015). Atmospheric mass loss during planet formation: the importance of planetesimal impacts. *Icarus*, 247, 81–94.
- Shornikov, S. I. (2015). Vaporization coefficients of oxides contained in the melts of Ca–Al-inclusions in chondrites. *Geochem. Int.*, 53, 1080–1089.
- Sossi, P. A., Klemme, S., O'Neill, H. S. C., Berndt, J., and Moynier, F. (2019). Evaporation of moderately volatile elements from silicate melts: experiments and theory. *Geochim. Cosmochim. Acta*, 260, 204–231.
- Sossi, P. A., Moynier, F., Treilles, R., Mokhtari, M., Wang, X., and Siebert, J. (2020). An experimentally-determined general formalism for evaporation and isotope fractionation of Cu and Zn from silicate melts between 1300 and 1500 °C and 1 bar. *Geochim. Cosmochim. Acta*, 288, 316–340.
- Tissandier, L., Libourel, G., and Robert, F. (2002). Gas-melt interactions and their bearing on chondrule formation. *Meteorit. Planet. Sci.*, 37, 1377–1389.
- Tsuchiyama, A., Tachibana, S., and Takahashi, T. (1999). Evaporation of forsterite in the primordial solar nebula; rates and accompanied isotopic fractionation. *Geochim. Cosmochim. Acta*, 63, 2451–2466.
- Urey, H. C. (1947). The thermodynamic properties of isotopic substances. Liversidge lecture, delivered before the Chemical Society in the Royal Institution on December 18th, 1946. *J. Chem. Soc.*, Resumed, 562–581. <https://doi.org/10.1039/jr9470000562>.
- Wang, J. H., Davis, A. M., Clayton, R. N., and Hashimoto, A. (1999). Evaporation of single crystal forsterite: evaporation kinetics, magnesium isotope fractionation, and implications of mass-dependent isotopic fractionation of a diffusion-controlled reservoir. *Geochim. Cosmochim. Acta*, 63, 953–966.
- Wimpenny, J., Marks, N., Knight, K., Borg, L., Badro, J., and Ryerson, F. (2020). Constraining the behavior of gallium isotopes during evaporation at extreme temperatures. *Geochim. Cosmochim. Acta*, 286, 54–71.
- Wimpenny, J., Marks, N., Knight, K., Rolison, J. M., Borg, L., Eppich, G., Badro, J., Ryerson, F. J., Sanborn, M., Huyskens, M. H., and Yin, Q.-Z. (2019). Experimental determination of Zn isotope fractionation during evaporative loss at extreme temperatures. *Geochim. Cosmochim. Acta*, 259, 391–411.
- Young, E. D., Galy, A., and Nagahara, H. (2002). Kinetic and equilibrium mass-dependent isotope fractionation laws in nature and their geochemical and cosmochemical significance. *Geochim. Cosmochim. Acta*, 66, 1095–1104.
- Young, E. D., Shahar, A., Nimmo, F., Schlichting, H. E., Schauble, E. A., Tang, H., and Labidi, J. (2019). Near-equilibrium isotope fractionation during planetesimal evaporation. *Icarus*, 323, 1–15.
- Yu, Y., Hewins, R. H., Alexander, C., and Wang, J. (2003). Experimental study of evaporation and isotopic mass fractionation of potassium in silicate melts. *Geochim. Cosmochim. Acta*, 67, 773–786.